Nanowire transistor arrays for mapping neural circuits in acute brain slices

Quan Qing[a,1], Sumon K. Pal[b,1], Bozhi Tian[a,1], Xiaojie Duan[a], Brian P. Timko[a], Tzahi Cohen-Karni[c], Venkatesh N. Murthy[b,2], and Charles M. Lieber[a,c,2]

[a]Department of Chemistry and Chemical Biology, [b]Molecular and Cellular Biology, Center for Brain Science, [c]School of Engineering and Applied Sciences, Harvard University, Cambridge, MA, 02138

Contributed by Charles Lieber, December 18, 2009 (sent for review December 15, 2009)

Revealing the functional connectivity in natural neuronal networks is central to understanding circuits in the brain. Here, we show that silicon nanowire field-effect transistor (Si NWFET) arrays fabricated on transparent substrates can be reliably interfaced to acute brain slices. NWFET arrays were readily designed to record across a wide range of length scales, while the transparent device chips enabled imaging of individual cell bodies and identification of areas of healthy neurons at both upper and lower tissue surfaces. Simultaneous NWFET and patch clamp studies enabled unambiguous identification of action potential signals, with additional features detected at earlier times by the nanodevices. NWFET recording at different positions in the absence and presence of synaptic and ion-channel blockers enabled assignment of these features to presynaptic firing and postsynaptic depolarization from regions either close to somata or abundant in dendritic projections. In all cases, the NWFET signal amplitudes were from 0.3–3 mV. In contrast to conventional multielectrode array measurements, the small active surface of the NWFET devices, $\sim 0.06\ \mu m^2$, provides highly localized multiplexed measurements of neuronal activities with demonstrated sub-millisecond temporal resolution and, significantly, better than 30 μm spatial resolution. In addition, multiplexed mapping with 2D NWFET arrays revealed spatially heterogeneous functional connectivity in the olfactory cortex with a resolution surpassing substantially previous electrical recording techniques. Our demonstration of simultaneous high temporal and spatial resolution recording, as well as mapping of functional connectivity, suggest that NWFETs can become a powerful platform for studying neural circuits in the brain.

multiplexed recording | nanodevice | neuron | patch clamp | silicon

Neural circuits are organized through synaptic connections into hierarchical networks operating on spatial and temporal scales that span multiple orders of magnitude (1). It is highly desirable to map the activities in large populations of neurons with both high position accuracy and precise timing. Advances in microfabrication of high-density passive multielectrode arrays (MEAs) (2) and active transistor arrays on silicon substrates (3) enable direct electrical recording down to *ca.* 10 μm length scales, although it is important to recognize that signals recorded within ∼100 μm are usually correlated (4–6). Specifically, in previous studies the device or electrode density defined by fabrication process, could be used to describe the true signal spatial resolution —that is the distance at which distinct signals can be resolved by adjacent detectors. Moreover, scaling down the size of individual metal electrodes to achieve more localized detection is difficult due to corresponding increases in their impedance (7, 8) that intrinsically limits the resolution of such passive recordings. Voltage- and calcium-sensitive optical dyes can provide excellent temporal and spatial resolution over wide fields (9, 10) but typically not simultaneously. For example, recent development of two-photon calcium imaging enables cellular/subcellular analysis in large populations of cells (11), yet reasonable temporal resolution for resolving single action potentials could only be achieved with reduced recording sites or compromised spatial resolution (12, 13), among other experimental challenges, for example, differential dye loading efficiency in different neurons (14).

In contrast, Si NWFET arrays have several features that make them unique for extracellular recording from neural circuits in acute brain slices. First, previous studies have shown that NWFETs can exhibit ultrahigh sensitivity detection of charged biomolecules (15, 16), including detection of single particles (17). Second, bottom-up fabrication of NWFETs yields devices that protrude from the substrate surface (18). This can reduce device to cell/tissue separation and promote enhanced cell-nanostructure interaction (19, 20), and has resulted in high signal to noise extracellular recording of action potentials from cultured cells (21–23) and cardiac tissue (24) with signals improved compared to planar FETs (22, 23). Third, the bottom-up approach also enables high-performance NWFET fabrication on transparent and flexible substrates (24) that facilitates high-resolution optical imaging at both surfaces of tissue samples, such as acute brain slices, and intracellular patch clamp measurements. The freedom to design device structures and arrays on substrates adapted to specific applications also opens up unique possibilities for interfacing with living tissues, for example, flexible silicon electronics (25) as well as bio-resorbable and implantable devices (26). Fourth, the active junction area of typical NWFETs, $0.06\ \mu m^2$, is much more localized and, thus, can provide better spatial resolution of signals compared to MEA and planar FETs that are 60 to 10^4 times larger in active area. In addition, the channel length of NWFETs can be reduced by at least two orders of magnitude as demonstrated previously (27), with a corresponding further decrease in active area. Last, NWFET detectors provide fast intrinsic response time for high temporal resolution recordings (28).

Results and Discussion

Experiment Approach and Signal Characterization. These NWFET features are exploited in our experiments illustrated in Fig. 1*A*. The pyramidal cell layer of an acute olfactory cortex slice is oriented over a specifically designed array of NWFETs on a quartz substrate chip, where the chip is assembled in a heating stage, with a perfusion chamber, allowing optical access in upright (Fig. 1*A*, *Inset*) or inverted microscopes during measurements. The spatial arrangement and density of the NWFET array is very flexible and can accommodate concurrent measurements across many different length scales, and a given device chip can be

---

Author contributions: Q.Q., S.K.P., B.T., V.N.M., and C.M.L. designed research; Q.Q., S.K.P., B.T., and X.D. performed research; Q.Q., S.K.P., B.T., X.D., B.P.T., T.C.-K., V.N.M., and C.M.L. analyzed data; and Q.Q., S.K.P., B.T., V.N.M., and C.M.L. wrote the paper.

The authors declare no conflict of interest.

[1]Q.Q., S.K.P., and B.T. contributed equally to this work.

[2]To whom correspondence may be addressed. E-mail: vnmurthy@fas.harvard.edu or cml@cmliris.harvard.edu

This article contains supporting information online at www.pnas.org/cgi/content/full/0914737107/DCSupplemental.

www.pnas.org/cgi/doi/10.1073/pnas.0914737107

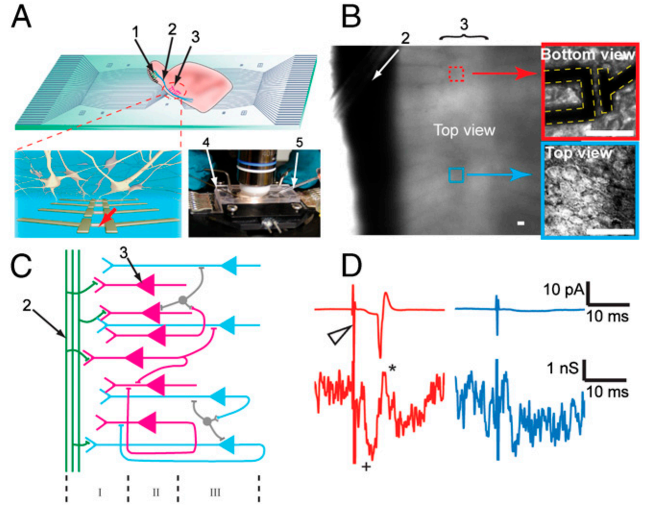

Fig. 1. (*A*) Measurement schematics. (*Top*) Overview of a NWFET array fabricated on a transparent substrate with slice oriented with pyramidal cell layer over the devices. (*Bottom Left*) Zoom-in of device region illustrating interconnected neurons and NWFETs. (*Bottom Right*) Photograph of the assembled sample chamber. *1*, *2*, and *3* indicate the mitral cells in the olfactory bulb, the lateral olfactory tract, and the pyramidal cells, resp. *4* and *5* mark the stimulation electrode and the patch clamp pipette, resp. (*B*) Top view of the NWFET array/brain slice region in fully assembled chamber with medium. *Red Box* shows a higher resolution image of a single device in contact with the neurons at the bottom of the slice. *Blue Box* shows the outermost neurons of the slice through an immersed lens from the top. Scale bars are 20 μm. (*C*) Laminar organization and input circuitry of the piriform cortex (*Layer I–III*). (*D*) Conductance recording from a NWFET (*Lower Traces*) in the same region as neuron used to record cell-attached patch clamp results (*Upper Traces*). Stimulation in the LOT was performed with strong (200 μA, *Red Traces*) and weak (50 μA, *Blue Traces*) 200 μs current pulses. The *Open Triangle* marks the stimulation pulse.

cleaned and used many times without degradation of the NWFET performance. One-dimensional and 2D arrays with device spacings of 80 and 60 μm, respectively (Fig. S1) as well as more complex arrays with 3–500 μm spacings were used in our experiments. An optical image of an oriented acute brain slice (Fig. 1*B*) shows the lateral olfactory tract (LOT) (*Dark Band*) and *Layer II* pyramidal neurons where individual cell bodies can be resolved at the upper surface for patch clamp studies and at the lower surface that is in contact with the NWFET devices. A schematic of the organization and input circuit of the slice in this region (Fig. 1*C*) highlights the myelinated axon fibers of the LOT and association fibers forming synaptic connections (*Layer I*) with the dendrites from the pyramidal cells in *Layer II* and *III*.

We characterized the basic response of the NWFET devices with simultaneous cell-attached-voltage-clamp and extracellular NWFET recordings in the same region of the slice (Fig. 1*D*), although the patched pyramidal neuron resides in the top layer versus bottom layer for the NWFET. Acute brain slices were prepared and handled by using standard procedures (29) as described in the *SI Text Methods*, and placed over the device chips in oxygenated artificial cerebrospinal fluid (aCSF). Based on the functional anatomy of the slice (1), layer II pyramidal cells located at any depth in the slice will behave similarly following LOT stimulation and, thus, the response recorded by the patch and NWFET should be similar. For a relatively strong stimulation of 200 μA (*Red Traces*) that will excite all neurons in the region, an action potential was clearly observed from the patch clamp (30). Correspondingly, the NWFET exhibited one peak temporally aligned with this action potential as well as features occurring at earlier times due to presynaptic firing and postsynaptic depolarization, as discussed below. When the intensity of stimulation is reduced below that required to elicit an action potential in the patched neuron, this peak is also lost from the NWFET recording although the postsynaptic depolarization is still observed (*Blue Traces*). We note that dead cells can be observed on some regions of the surface of the brain slice, although they do not uniformly cover the entire slice and, moreover, it is straightforward to locate and patch healthy pyramidal cells on the outermost layer.

To define further the characteristics of the NWFET signals recorded at different positions, we made measurements in the absence and presence of synaptic and ion-channel blockers. All traces were reproducibly observed in all of our experiments, and the neuronal signals could be easily recognized without additional filtering or averaging. However, to more accurately identify the characteristics of these neuronal peaks, for example, the timing and peak width, especially when comparing across different devices, raw traces were averaged to minimize error introduced by noise. A representative overlay of raw data traces and the corresponding averaged result are presented in the Fig. S2 to show that all signals presented in this work are reproducible and not isolated events. Two basic types of reproducible time-dependent signals were recorded with the NWFET devices following stimulation of the LOT. In the first (Fig. 2*A*, *B*) there is a broad peak representing a decrease of conductance followed by second peak corresponding to a conductance increase, noting that the latter demonstrates a stimulation intensity threshold behavior, in accordance with the action potential recorded in cell-attached patch measurements. In addition, there are also sharper peaks corresponding to decrease and increase of conductance within *ca.* 2 ms of the stimulation event. The second type of trace (Fig. 2*C*, *D*) exhibits a broad peak representing increase of conductance that decreases with modulations over 10–15 ms time scale as well as sharper peaks corresponding to decrease and increase of conductance within *ca.* 2 ms of the stimulation event.

Addition of 6-cyano-7-nitroquinoxaline-2,3-dione (CNQX) and D(-)-2-Amino-5-phosphonopentanoic acid (APV), which block α-amino-3-hydroxyl-5-methyl-4-isoxazole-propionate (AMPA-) and N-methyl-D-aspartic acid (NMDA-) receptor mediated glutamatergic transmission (31), leads to the elimination of the broad conductance decrease and subsequent increase in Fig. 2*A*, *B* and the broad conductance peak in Fig. 2*C*, *D*. In both cases, the fast peaks following stimulation are unchanged by adding CNQX-APV. Hence, we can unambiguously conclude that signals eliminated correspond to postsynaptic processes, including action potential (marked by *) and excitatory postsynaptic potential (EPSP, marked by +), while the early time peaks (<2 ms following stimulation) are presynaptic activity, such as fiber volley from the LOT. The addition of tetrodotoxin (TTX) resulted in elimination of the short time peaks (Fig. 2*A*, *B*, *Third Traces*) as expected for blockage of all fast sodium channels. Last, we note that all blocker tests were reversible after washout with medium.

The conductance change of the NWFET directly reflects the extracellular potential changes from a local region of pyramidal cells, as demonstrated in previous studies (21–24). By comparing our results to the extracellular recordings with metal electrodes (1), we can confirm the peak assignments based on threshold and blocker experiments above, and correlate the different polarities of observed signals with the components of the slice in the region under detection (Fig. 2*E*). When a NWFET is close to the somata of pyramidal neurons, the extracellular potential first exhibits a positive EPSP, followed by the population spike (p-spike) from the action potential that appears as a fast, negative peak. Because the conductance of p-type NWFET decreases when external potential increases, this leads to inversion of signals with respect to extracellular potential recorded by a metal electrode. Similarly, when the NWFET resides in a region abundant in dendritic projections, it would sense a broad negative

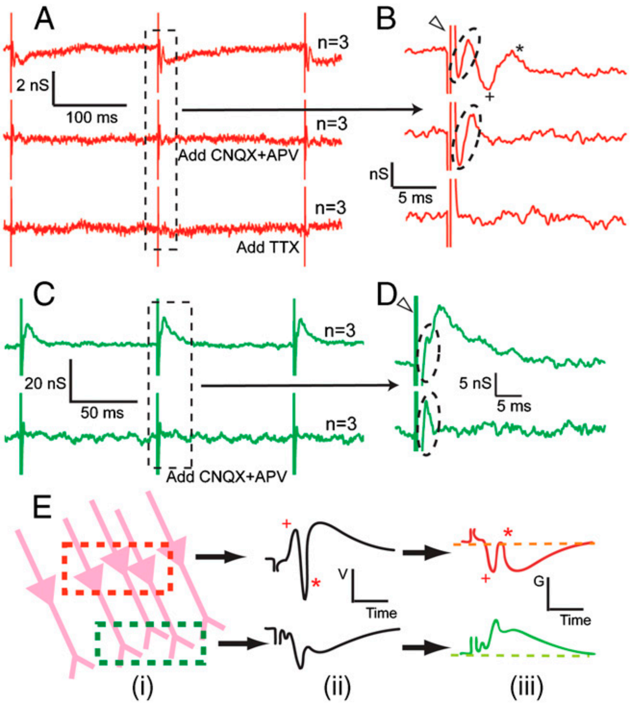

Fig. 2. Characteristics and identification of NWFET signals. (*A*) Conductance vs. time traces from NWFET devices, where each trace has three stimulation events. The *Top*, *Middle*, and *Bottom Curves* correspond to data recorded initially, after the addition of CNQX and APV and after the addition of TTX, resp. Traces are average of three consecutive recordings ($n = 3$). (*B*) Expansion of region indicated by *Dashed Frame* of (*A*) The *Open Triangle* and *Dashed Oval* mark the stimulation and presynaptic features, resp. The *Plus* and *Asterisk* mark the postsynaptic features. (*C*) NWFET conductance vs. time trace recorded in a different position. The *Top* and *Bottom Curves* correspond to data recorded initially and after the addition of CNQX and APV, resp. (*D*) Zoom-in for region indicated by the *Dashed Frame* in (*C*). (*E*) Model explaining different recorded signals. From left to right: (*i*) Detection region overlapping with cell bodies (*Red Frame*) or dendrites (*Green Frame*); (*ii*) extracellular potential following stimulation exhibits opposite polarities (p-spike is marked by *, and the EPSP is marked by +) in these regions; and (*iii*) corresponding conductance change of p-type Si NWFET.

potential change with less significant p-spike on the tail, which results in a positive conductance change for the NWFET, as seen in Fig. 2*C*, *D*. In addition, the conductance response of the NWFETs, when converted to external potential change using the sensitivity of the devices (22, 24), corresponds to 0.3–3 mV extracellular signals. However, these potentials should not be directly compared to reported MEA measurements (4–6), because the scales of active regions are completely different. There would be no signal from an MEA electrode of comparable size to our nanodevices.

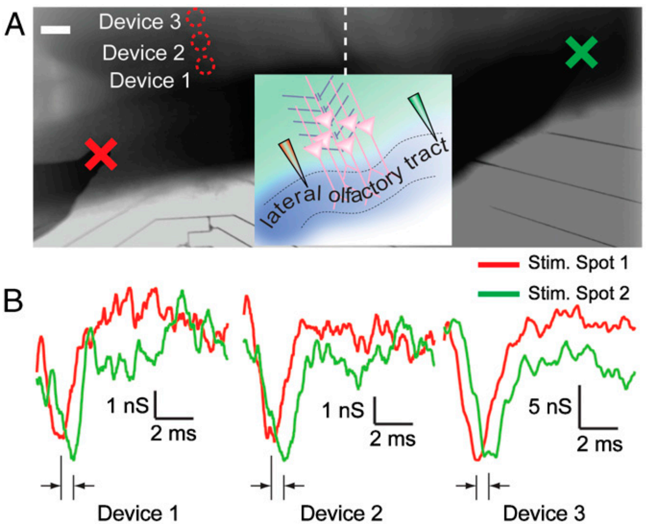

Fig. 3. Measurement of signal propagation in LOT with 1D device array. (*A*) Optical image of the brain slice covering the 1D NWFET array. The 1D array is aligned perpendicularly to the LOT fiber. The *Red Circles* mark the positions of *Devices 1–3* used for recording. The stimulation electrode is positioned at spot one (*Red Cross*), which is *ca.* 400 μm away from the array and spot two (*Green Cross*), which is *ca.* 1200 μm on the other side. The image is a composite of recorded micrographs. The *Dash Line* marks the border of the original pictures. The scale bar is 100 μm. *Inset* is a schematic of experimental configuration. (*B*) NWFET conductance traces from *Devices 1–3* when stimulating at spot one (*Red*) and two (*Green*). Data are averaged from eight recordings.

Spatiotemporal Resolution of NWFET Recordings. The above results show that the NWFETs fabricated on transparent substrates can record robust extracellular signals from the acute olfactory brain slices with good temporal and spatial resolution but do not define the limits of temporal-spatial resolution. To address temporal resolution, we first used a 1D NWFET array to measure signal propagation rates in the LOT. The slice was placed over the 1D device array with the myelinated axon fibers in LOT orthogonal to the NWFET array (Fig. 3*A*). The stimulation peak or artifact (3) was used to accurately align and compare the signals from different devices and tests, and the depolarization peak of the EPSP was used to mark the time when the stimulation reaches the neurons. Signals recorded from three NWFET devices following stimulation at positions *ca.* 400 μm to the left and *ca.* 1200 μm to the right (Fig. 3*B*) showed clear signal delays when the stimulator was farther from the NWFET array. Device 1–3 showed time lags of 0.5 ± 0.2, 0.4 ± 0.2, and 0.4 ± 0.2 ms, resp., where the delay corresponds to the time for the signal to travel through the 800 μm length difference of the myelinated axon fibers (assuming symmetric connections from the neurons over the NWFETs to the LOT on both sides of the device array). We note here that the signals from all devices did not overlap with each other and showed different timing from the stimulation pulses. This observation rules out the possibility of cross talk between the devices. The similar results recorded from all three NWFETs are consistent with the topology of the pyramidal cell connections close to the LOT (Fig. 1*C*) and demonstrate the reproducibility of the NWFET measurements. The timing differences yield a propagation rate of 1.6–2 m/s in the LOT, which is consistent with reported values for myelinated axons (32), and show that NWFET arrays can be used to resolve reliably signal timing that reflects true signal path with sub-millisecond temporal resolution.

Second, multiplexed recording by using device arrays fabricated with NWFET spacings from 3–500 μm allowed us to determine the highest resolution where signals of different characteristics can still be distinguished. For example, we made recordings from slices by using six NWFETs (Fig. 4*A*) where the separations between devices 1 and 2, 3 and 4, and 5 and 6 was 3, 5 and 8 μm, resp., and devices 1 and 2 were 30 μm from 3 and 4, and devices 5 and 6 were 120 μm from 1–2/3–4. Following higher intensity stimulation of the LOT (Fig. 4*b*, *Left*) devices 1 and 2 displayed weak negative conductance response, whereas device 3–6 gave strong positive peaks. The polarity and amplitude differences between devices 1 and 2 and 3 and 4 showed that the details within 30 μm, the scale of a single neuron, could be clearly resolved, possibly arising from recording at the soma versus the dendrite projection. Interestingly, at a reduced stimulation intensity (Fig. 4*B*, *Right*) the signal from device 4 was almost undetectable, whereas device 3, which was only 5 μm away, still yielded a clear peak. This difference cannot simply be attributed

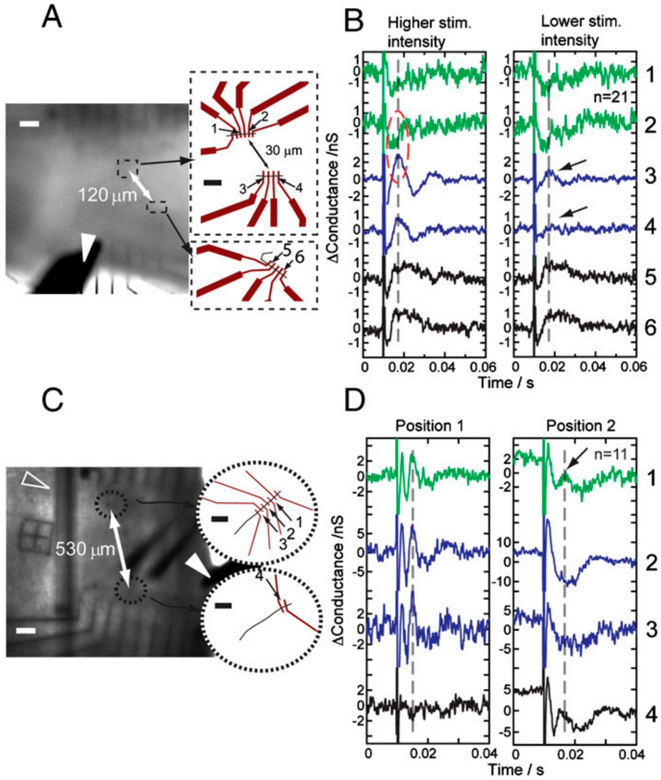

Fig. 4. Localized detection with NWFET arrays. (*A*) (*Left*) Optical image of brain slice over Si NWFET arrays defined by electron-beam lithography. The *Dashed Frames* mark the positions of *Devices 1–4* and *5* and *6*. (*Right*) Schematics of the devices. (*B*) Signals obtained from *Devices 1–6* with 200 μs stimulation of 2.5 (*Left*) and 1 mA (*Right*); $n = 21$. The *Dashed Oval* marks the region where signals of opposite polarity were recorded from devices 30 μm apart. (*C*) (*Left*) Optical image of brain slice over different design NWFET array. The *Dashed Circles* mark positions of *Devices 1–3* and *Device 4*. (*Right*) Schematics of the devices. (*D*) Signals obtained from *Devices 1–4* with stimulation of 1 mA, 200 μs, averaged from $n = 11$ recordings. The *Arrows* mark one device picking up a signal; the other 5 μm away does not. The *White* and *Black Scale Bars* in (*A*) and (*C*) are 100 and 10 μm, resp. The *Open Triangles* and *Filled Triangles* in (*A*) and (*C*) mark the fine anchor thread used to hold the slice over the device chip and the stimulator, resp. The DC component was removed from traces (1–3 kHz bandpass) shown in (*B*) and (*D*).

to differing device sensitivities, and suggests potential for resolution of signals with distinct characteristics with a resolution higher than 10 μm.

The ability to record extracellular signal contrast on such small length scales is robust and was further investigated in experiments with a second device array (Fig. 4*C*) in which devices 1–3 were evenly separated by 5 μm, and device 4 was further separated by 530 μm. These devices were used to record signals at different positions in the piriform cortex at fixed stimulation intensity. In many cases (e.g., Fig. 4*D*, *Position 1*), devices 1–3 gave signals of the same shape and amplitude, which shows that there were no intrinsic differences across these devices. However, when the array position was changed (Fig. 4*D*, *Position 2*), device 1 displayed a peak corresponding to action potential and devices 2 and 3 only gave the broad signal correlating to EPSP discussed above. These results, thus, indicate a 5 μm resolution of distinct signals. We note that device 4 showed the same characteristics as device 1 at *Position 2* with ∼1 ms time shift, demonstrating that the stimulation intensity was sufficient to elicit firing in a region encompassing all of the devices. The different noise level in the baseline of the devices may be a result of variation of device performance as well as local neuron activities that are not directly correlated with the stimulation (after averaging).

The high-resolution recording of distinct extracellular signals achieved in the above experiments exceeds that reported in previous MEA and FET recording studies of acute brain slices (4–6, 33). In planar MEA and FET studies of brain slices, current sources/sinks from neural activity distant from the device detection plane are reconstructed (34), although this can be limited due to (*i*) missing out-of-plane distances (33), (*ii*) averaging by active device area comparable to the size of a cell body, and (*iii*) complex contacts to acute slice preparation that are not idealized parallel planes. The subcellular resolution observed in our new work suggests that our nanoscale, nanostructured detectors, which are comparable in size to synaptic connections and can promote tissue-device interactions (19, 20), provide the direct capability for high-resolution signal mapping.

Exceptionally high resolution was not obtained universally at all positions. This observation is consistent with results above where we found surface regions that had or were free from dead cells that may partially isolate the nanodevices from the signal source. We believe that our optimization of the bottom-up fabrication of the NWFETS, so that they protrude further for device chip surface, can overcome this variability of brain slice preparation and, thus, provide consistently high-resolution recording in the future. In addition, detailed modeling of the high-resolution signals recorded by NWFETs will be required to better understand and potentially quantify absolute amplitude of recorded signals (e.g., slice-to-slice variations may explain changes in recorded amplitude), although the results themselves already provide robust information relevant to understanding and quantifying complex connectivity in the brain slices. Specifically, the relative amplitude, shape, and timing of signals from NWFET devices, in an array under consistent test conditions on the same brain slice, can provide a robust measure of neural activities and, hence, functional circuitry. We elaborate on this important capability below.

2D NWFET Arrays Map Neural Connectivity in the Olfactory Cortex. We have exploited the high-resolution recording capability of NWFETs in 2D arrays to probe the activity patterns of layer II/III cells in the piriform cortex when stimulating different sets of axon fibers in the LOT. In a representative experiment (Fig. 5*A*), eight devices within a four-by-four array oriented under the pyramidal cell layer of an acute slice were simultaneously monitored following stimulation at eight different spots (*A–H*) in the LOT. Strong stimulation of all axons fibers in the LOT (Fig. 5*B*) yielded similar response by NWFETs 1–8 with clear p-spike signals regardless of stimulation positions. Blocker tests further confirmed that these signals were all due to postsynaptic activity (Fig. S3). A 2D map of the recorded activity (*SI Text Methods*) provides a ready visualization of relatively uniform response in this region of the olfactory cortex to the strong stimulation.

To evaluate the ability to detect sparse patterns of activity, the stimulation intensity was reduced so that at each spot only a subgroup of fibers was activated. As an example, recordings from *Devices 1* and *8* for stimulation positions *A–H* (Fig. 5*C*) exhibit the p-spike peak only with stimulation at device-specific sites. We note that binning the individual traces for a given device and comparing distinct averages (e.g., odd vs. even) produced similar results in all cases and, thus, show that observed differences are robust. We summarize the results from all eight devices in the array as 2D activity maps for each of the eight stimulation positions (Fig. 5*D*). Notably, visual inspection of these maps demonstrates clearly how heterogeneous activity can be resolved. For example, stimulation spot *B* is strongly coupled to most regions except that monitored by *Device 1*, stimulation spot *F* is weakly coupled to most regions, and visual comparison also shows very different pairwise correlations for activity at different stimulation points. To quantify this latter important point, we plotted the correlated activities recorded by two well-separated devices, *1* and *8*,

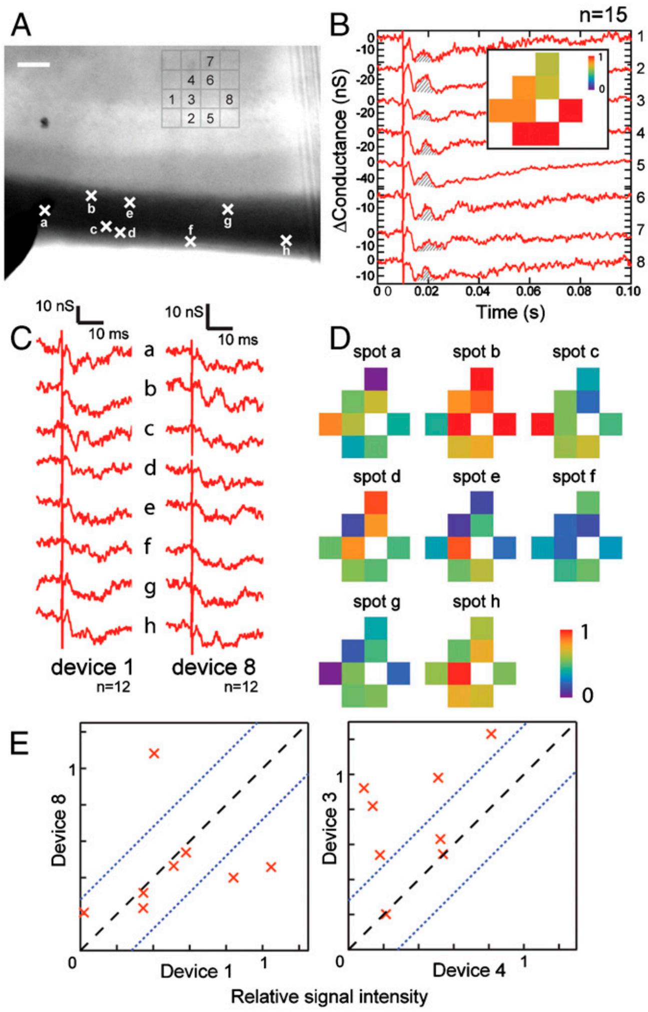

Fig. 5. Two-dimensional mapping of heterogeneous activities in the pyramidal cell layer. (*A*) Optical image of an acute slice over a 4 × 4 NWFET array. Signals were recorded simultaneously from the eight devices indicated on the image. Crosses along the LOT fiber region of the slice mark the stimulation spots *A*–*H*. The stimulator insertion depth was not controlled precisely in these experiments. Scale bar represents 100 μm. (*B*) Signals recorded for devices 1–8 when stimulated with a 200 μs 400 μA pulse. Data are averaged from 15 recordings. The *Shaded Area* in each trace corresponds to the p-spike and was used to obtain normalized intensity (*SI Text Methods*). *Inset*: normalized map of the signal intensity from the 8 Devices. (*C*) Representative signals recorded from Devices 1 and 8 when stimulating at spots *A*–*H* with 200 μs and 100 μA pulses. Data are averaged from 12 recordings. (*D*) Maps of the relative signal intensity or activity for devices 1–8. (*E*) Correlation between Devices 1 and 8 (*Upper Plot*) and Devices 3 and 4 (*Lower Plot*) for the different stimulation positions. The *Dashed Black Line* marks signals that are correlated. The *Dotted Blue Lines* mark the uncertainty due to device signal fluctuations determined from correlation analysis (*SI Text Methods*).

and two adjacent devices, *3* and *4* (Fig. 5*E*), where bounds on the experimental uncertainty are placed by using "self-correlation" for the devices (*SI Text Methods*). Significantly, we find that the signals from Devices 1 and 8, which are from the same layer of pyramidal cells, show close correlation for 5/8 stimulation points, and low correlation for the remaining 3 points. In contrast, signals from the adjacent Devices 3 and 4 show close correlation for only 3/8 stimulation points. We note that the distance between adjacent devices (60 μm) in which distinct activity has been readily recorded is already better than the ∼100 μm scale where signals from MEA approaches exhibit correlation. Given the highly localized detection (<10 μm) demonstrated above, the mapping resolution can be substantially improved in the future.

Conclusions

Our results demonstrate that the NWFET arrays detect local activity of the pyramidal cell layer and LOT on at least the 10 μm scale and, thus, can be used to understand the functional connectivity of this region. The scale of local detection contrast interdependent extracellular signals recorded from neighboring regions on even larger (∼100 μm) length scales by using MEAs (4–6). While it will be important to further describe the spatial and temporal limits of our NWFET arrays for acute brain slice recording, we believe that these results show clearly the potential of this tool for addressing critical biological problems. For example, the non-topographic fashion of fiber projection from the olfactory bulb to the cortex makes fine anatomic analysis of connections across functional regions difficult (35, 36) and, whereas retrograde labeling and transneuronal genetic tracing can potentially provide necessary anatomical information, the functional connectivity of the olfactory cortex remains largely unknown (37). Furthermore, the plasticity of olfactory system suggests that the network is highly dynamic. Thus, highly localized direct recording of ensembles of neurons in the context of spatially resolved stimulation could serve as a powerful tool to visualize the dynamic, functional connection map and provide information necessary to understand the circuits and plasticity in this and other neural systems.

In addition, the high input impedance of the NWFETs circumvents the common challenge confronted by implanted microelectrodes, where post-implant increases of impedance due to, for example, absorption of proteins, leads to degraded signal quality and higher noise level (38). This makes NWFETs very promising for high signal yield, chronic in vivo recordings, especially considering the facts that (*i*) small device feature size allows multiplexed detectors being integrated onto ultrasmall probes for minimum damage to the tissue, (*ii*) bottom-up fabrication makes it possible to choose biocompatible materials as substrates to reduce mechanical mismatch and to minimize reactive tissue response (25, 26), and (*iii*) the nanoscale morphology could promote better attachment of active neurons, leading to better signal quality than planar designs. Therefore, NWFETs could also bring exciting and unique opportunities to interfacing living tissue and electronics.

Materials and Methods

The 30 nm diameter silicon NWs were synthesized by gold nanocluster catalyzed chemical vapor deposition as described previously (39). NWFET devices were fabricated on quartz substrates by aligning NWs on the surface (40), photo- or electron-beam lithography patterning, and deposition of Ti/Pd/Ti (1.5/60/5 nm) as contacts. Contacts were passivated with 60 nm Si_3N_4 and 2 μm thick SU-8 polymer (Microchem). Modified parasigittal slices (300–500 μm) containing both the olfactory bulb and piriform cortex were prepared from rats (postnatal day 17–20) using standard procedures (29). All animal procedures conformed to US National Institutes of Health guidelines and were approved by Harvard University's Animal Care and Use Committee. Slices were placed in contact with the substrate in oxygenated artificial cerebrospinal fluid (aCSF) and the pyramidal cell layer was aligned over the device region. No additional steps were taken to enhance adhesion of the tissue to NWs or substrate. NW recording was carried out in perfusion of aCSF with a 150 mV DC source voltage. The current was amplified with a home-built multi-channel current/voltage preamplifier, filtered with a 1 Hz–3000 Hz signal conditioner (CyberAmp 380), and digitized at 20 KHz sampling rate (Axon Digi1440A). Patch clamp was performed with an Axopatch 200B from Molecular Device Systems using glass pipettes pulled on a P-97 Flaming/Brown Micropipette Puller (Sutter Instruments). Concentric bipolar Pt/Ir electrodes with diameter of 200 μm/50 μm (outer/inner, FHC, Inc.) were used to stimulate the LOT. Bipolar current pulses (duration 200 μs, amplitudes 50 μA to 2.5 mA) were generated by a Model 2100 Isolated Pulse Stimulator from A-M Systems.

ACKNOWLEDGMENTS. C.M.L. acknowledges support from a NIH Director's Pioneer Award and the McKnight Foundation Neuroscience Award.

1. Shepherd GM (2004) *The Synaptic Organization of the Brain* (Oxford Univ Press, Inc., New York), Ch. 1, 5, 10, 11, 5th Ed.
2. Taketani M, Baudry M (2006) *Advances in Network Electrophysiology Using Multi-Electrode Arrays* (Springer Science+Business Media, Inc., New York).
3. Hutzler M, et al. (2006) High-resolution multitransistor array recording of electrical field potentials in cultured brain slices. *J Neurophysiol*, 96:1638–1645.
4. Egert U, Heck D, Aertsen A (2002) Two-dimensional monitoring of spiking networks in acute brain slices. *Exp Brain Res*, 142:268–274.
5. Wirth C, Lüscher HR (2004) Spatiotemporal evolution of excitation and inhibition in the rat barrel cortex investigated with multielectrode arrays. *J Neurophysiol*, 91:1635–1647.
6. Frey U, Egert U, Heer F, Hafizovic S, Hierlemann A (2009) Microelectronic system for high-resolution mapping of extracellular electric fields applied to brain slices. *Biosens Bioelectron*, 24:2191–2198.
7. Prohaska OJ, Olcaytug F, Pfundner P, Dragaun H (1986) Thin-film multiple electrode probes: Possibilities and limitations. *IEEE T Bio-Med Eng*, BME-33:223–229.
8. Banks DJ, Balachandran W, Richards PR, Ewins D (2002) Instrumentation to evaluate neural signal recording properties of micromachined microelectrodes inserted in invertebrate nerve. *Physiol Meas*, 23:437–448.
9. Grinvald A, Hildesheim R (2004) VSDI: A new era in functional imaging of cortical dynamics. *Nat Rev Neurosci*, 5:874–885.
10. Rochefort NL, Jia H, Konnerth A (2008) Calcium imaging in the living brain: Prospects for molecular medicine. *Trends Mol Med*, 14:389–399.
11. Stosiek C, Garaschuk O, Holthoff K, Konnerth A (2003) In vivo two-photon calcium imaging of neuronal networks. *P Natl Acad Sci USA*, 100:7319–7324.
12. Reddy GD, Kelleher K, Fink R, Saggau P (2008) Three-dimensional random access multiphoton microscopy for functional imaging of neuronal activity. *Nat Neurosci*, 11:713–720.
13. Holekamp TF, Turaga D, Holy TE (2008) Fast three-dimensional fluorescence imaging of activity in neural populations by objective-coupled plannar illumination microscopy. *Neuron*, 57:661–672.
14. Yuste R, Konnerth A (2005) *Imaging in Neuroscience and Development: A Laboratory Manual* (Cold Spring Harbor Laboratory Press, Cold Spring Harbor, NY).
15. Zheng GF, et al. (2005) Multiplexed electrical detection of cancer markers with nanowire sensor arrays. *Nature Biotechnol*, 23:1294–1301.
16. Stern E, et al. (2007) Label-free immunodetection with CMOS-compatible semiconducting nanowires. *Nature*, 445:519–522.
17. Patolsky F, et al. (2004) Electrical detection of single viruses. *P Natl Acad Sci USA*, 101:14017–14022.
18. Patolsky F, Timko BP, Zheng GF, Lieber CM (2007) Nanowire-based nanoelectronic devices in the life sciences. *MRS Bull*, 32:142–149.
19. Zhou XJ, Moran-Mirabal JM, Craighead HG, McEuen PL (2007) Supported lipid bilayer/carbon nanotube hybrids. *Nature Nanotechnol*, 2:185–190.
20. Cellot G, et al. (2009) Carbon nanotubes might improve neuronal performance by favouring electrical shortcuts. *Nature Nanotechnol*, 4:126–133.
21. Patolsky F, et al. (2006) Detection, stimulation, and inhibition of neuronal signals with high-density nanowire transistor arrays. *Science*, 313:1100–1104.
22. Cohen-Karni T, Timko BP, Weiss LE, Lieber CM (2009) Flexible electrical recording from cells using nanowire transistor arrays. *P Natl Acad Sci USA*, 106:7309–7313.
23. Eschermann JF, et al. (2009) Action potentials of HL-1 cells recorded with silicon nanowire transistors. *Appl Phys Lett*, 95:083703–1–083703–3.
24. Timko BP, et al. (2009) Electrical recording from hearts with flexible nanowire device arrays. *Nano Lett*, 9:914–918.
25. Kim D, et al. (2008) Strechable and foldable silicon integrated circuits. *Science*, 320:507–511.
26. Kim D, et al. (2009) Silicon electronics on silk as a path to bioresorbable, implantable devices. *Appl Phys Lett*, 95:133701–1–133701–3.
27. Wu Y, Xiang J, Yang C, Lu W, Lieber CM (2004) Single-crystal metallic nanowires and metal/semiconductor nanowire heterostructures. *Nature*, 430:61–65.
28. Hu Y, Xiang J, Liang G, Yan H, Lieber CM (2008) Sub-100 nanometer channel length Ge/Si nanowire transistors with potential for 2 THz switching speed. *Nano Lett*, 8:925–930.
29. Tyler WJ, Petzold GC, Pal SK, Murthy VN (2007) Experience-dependent modification of primary sensory synapses in the mammalian olfactory bulb. *J Neurosci*, 27:9427–9438.
30. Perkins KL (2006) Cell-attached voltage-clamp and current-clamp recording and stimulation techniques in brain slices. *J Neurosci Meth*, 154:1–18.
31. Blake JF, Brown MW, Collingridge GL (1988) CNQX blocks acidic amino acid induced depolarizations and synaptic components mediated by non-NMDA receptors in rat hippocampal slices. *Neurosci Lett*, 89:182–186.
32. Andersen P, Soleng AF, Raastad M (2000) The hippocampal lamella hypothesis revisited. *Brain Res*, 886:165–171.
33. Stangl C, Fromherz P (2008) Neuronal field potential in acute hippocampus slice recorded with transistor and micropipette electrode. *Eur J Neurosci*, 27:958–964.
34. Mitzdorf U (1985) Current source-density method and application in cat cerebral cortex: Investigation of evoked potentials and EEG phenomena. *Physiol Rev*, 65:37–100.
35. Devor M (1976) Fiber Trajectories of olfactory bulb efferents in the hamster. *J Comp Neurol*, 166:31–48.
36. Scott JW, McBride RL, Schneider SP (1980) The organization of projections from the olfactory bulb to the piriform cortex and olfactory tubercle in the rat. *J Comp Neurol*, 194:519–534.
37. Martinez-Marcos A (2009) On the organization of olfactory and vomeronasal cortices. *Prog Neurobiol*, 87:21–30.
38. Mercanzini A, Colin P, Bensadoun JC, Bertsch A, Renaud P (2009) In vivo electrical impedance spectroscopy of tissue reaction to microelectrode arrays. *IEEE T Bio-Med Eng*, 56:1909–1918.
39. Wu Y, et al. (2004) Controlled growth and structures of molecular-scale silicon nanowires. *Nano Lett*, 4:433–436.
40. Javey A, Nam S, Friedman RS, Yan H, Lieber CM (2007) Layer-by-layer assembly of nanowires for three-dimensional, multifunctional electronics. *Nano Lett*, 7:773–777.